




Fabrication of right triangular prism retroreflectors through $3\frac{1}{2}\frac{1}{2}$ -axis ultraprecise single point inverted cutting

Benjamin W. Hamilton ^a, Sama Hussein ^a, Nicolas Milliken ^a, O. Remus Tutunea-Fatan ^a and Evgueni V. Bordatchev ^b

^aWestern University, London, Canada; ^bNational Research Council of Canada, Canada

ABSTRACT

Retroreflectors (RR) are passive optical structures that are capable of returning incident light back to the source. The focus of the current study is represented by the right triangular prism (RTP) geometry which could be a more efficient alternative to the traditional inverted corner cube geometry. While current manufacturing practices rely solely on the use of conventional pin-bundling techniques, the work reported in this study presents further enhancements of the previously introduced ultraprecise single point inverted cutting technique which can be used in a manner approximately similar to $3\frac{1}{2}\frac{1}{2}$ -axis kinematics. The experimental results obtained have demonstrated both the feasibility of the proposed fabrication approach as well as the optical viability of the fabricated RTP elements.

KEYWORDS

Automotive lighting; retroreflector design; optical performance; $3\frac{1}{2}\frac{1}{2}$ -axis diamond cutting

1. Introduction

A retroreflector (RR) is a passive optical device that reflects light back to the originating source through a range of incident angles deviating from the normal axis. RRs can be divided into two categories: lens-and-mirror, and inverted corner cube (ICC). As depicted in Fig. 1a, the lens-and-mirror type, also referred to as cat's eye, are made of transparent spheres with a reflective layer on the back. The sphere has a refractive index greater than air which causes the light entering the sphere to be directed to the reflective surface. The reflected light is then refracted again as it leaves the sphere and because of that it ends up traveling in a direction that is parallel to that of the incident light [8]. Alternatively, the ICC retroreflector consists of three mutually orthogonal surfaces each contributing to retroreflection (Fig. 1b). In case of this retroreflective element, the incident light reflects off each facet and after three successive reflections will be reflected back to the source according to a phenomenon called total internal reflection (TIR) [11]. More details about the construction and functionality of RRs can be found in [3,11].

Retroreflective arrays have found many industrial applications, including, but not limited to traffic safety, communications, and metrology. Moreover, its superior efficiency at long distances makes the ICC appropriate for the needs of the automotive industry [8] and the typical

example in this category is represented by the taillights installed on virtually all transportation vehicles [11].

However, the fabrication of the corner cube geometry poses an inherent challenge in a sense that rotating tools cannot be used to produce the geometry of the ICC, particularly around its apex. Because of this, the “workaround” that has been in use for several decades involves the use of the pin-bundling technique [16]. According to this method, the “negative” (e.g. the core) of each RR element in the array is formed by means of the end of a hexagonal pin that in turn is produced through conventional machining followed by lapping in order to attain the $R_a < 10$ nm surface finish that is required for optical reflectivity. Once individual pins are completed, they are bundled together and a cavity insert is created at their forming end by means of electroforming.

Its inherent complexity makes pin-bundling inefficient, error-prone and difficult to use for microscale features, particularly due to the stringent surface quality requirements calling for $R_a < 10$ nm, a requirement which is typically equated with optical surface quality. For this reason, more efficient and versatile retroreflector fabrication techniques are highly desirable and two new ideas have recently emerged in this regard: i) development of cutting/machining-based fabrication techniques and ii) development of alternate RR shapes, preferably of lower geometric complexity.

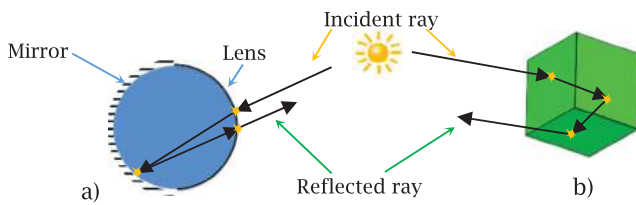


Figure 1. Functionality of typical RR elements: a) lens-and-mirror, and b) inverted corner cube.

In response to these challenges, a new fabrication process called ultraprecise single point inverted cutting (USPIC) along with a novel RR geometry coined as right triangular prism (RTP) have been recently developed [6,7] as viable alternatives to pin-bundling fabrication and ICC RR design, respectively. However, while the initial experiments proved that USPIC can produce the desired RTP geometry [6], it also became clear that the combination of plunging and ploughing motions that can be generated through the sole involvement of the translational axes of a five-axis machine is insufficient to attain the intended optical surface quality. To address this, the primary goal of the current study was to fabricate the new RTP geometry through a combination of translational and rotational motions, for which purpose the development of an USPIC postprocessor becomes essential.

2. Design and optical performance of RTP arrays

2.1. Optical characterization of the RTP element

To ensure the retroreflective functionality of the novel RTP geometry, its geometry was modeled in CAD and then subjected to optical simulation analysis performed with a specialized software. The geometry of an RTP includes two reflective facets with role in TIR and one incident facet/aperture through which light enters and then exits (Fig. 2). According to the automotive use of the RRs, an illumination element whose size is determined

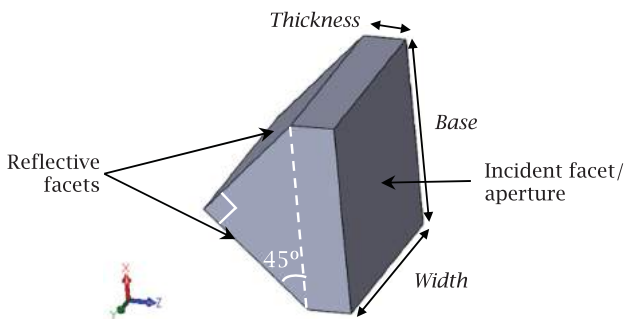


Figure 2. Geometry of the RTP element.

by *thickness*, *width* and *base* was joined with the incident face of the RTP.

To assess the optical performance of the new RTP design, the retroreflective efficiency (RRE) – defined as the percentage ratio of retroreflected light to incidence light – was determined through a series of optical simulations in which the primary variable was the direction of the incident beam (Fig. 3). The optical simulation model (Fig. 3a) included an RTP element with a rectangular aperture of 0.45×0.45 mm, a light source with a rectangular shape matching that of the RTP aperture, as well as a detector capable to measure the quantity of the retroreflected light. The material assumed for RTP element was polymethyl methacrylate (PMMA).

To verify the retroreflective capabilities of the RTP, the light source was tilted to cover a range of incident angles between -40° and $+40^\circ$ and it was also simultaneously shifted vertically up and down in order to ensure the aforementioned areal matching between RTP's aperture and that of the rectangular-profiled light source. The incoherent irradiance (W/cm^2) of the retroreflected light acquired by the detector was used to calculate the RRE corresponding to 1 W of light projected at various incidence angles. A larger 5° increment was used to scan the -40° to $+40^\circ$ range, while a smaller/finer 1° increment was used between -5° and $+5^\circ$.

The results presented in Fig. 3b reveal that as the incidence angle increases, the RRE of the RTP element decreases since more light is lost either because it is reflected at the incident face of the illumination element or because it is never returned in the direction of the observer/detector. As such, these results imply that the best optical performance occurs when RTP's incident face is normal to the incident light. However, this theoretically "ideal" RR may not be in fact suitable for automotive lighting applications as it returns the incident light back to its source whereas this location may or may not coincide with the actual position of the observer.

2.2. Automatic CAD-based generation of the RTP array

As mentioned previously, a RR surface can be created by arranging individual RTP elements in an arrayed pattern. The base surface, in which the RTP cavities are fabricated, could have any freeform shape (i.e. automotive taillights), but has been assumed planar in our study to simplify the geometry. The pattern and orientation of each structure could also take on many forms, but has assumed a brick-like pattern (Fig. 4). Geometry is characterized by parameters which indicate the size of the array, individual element size, and how each element is positioned and oriented with respect to neighboring elements.

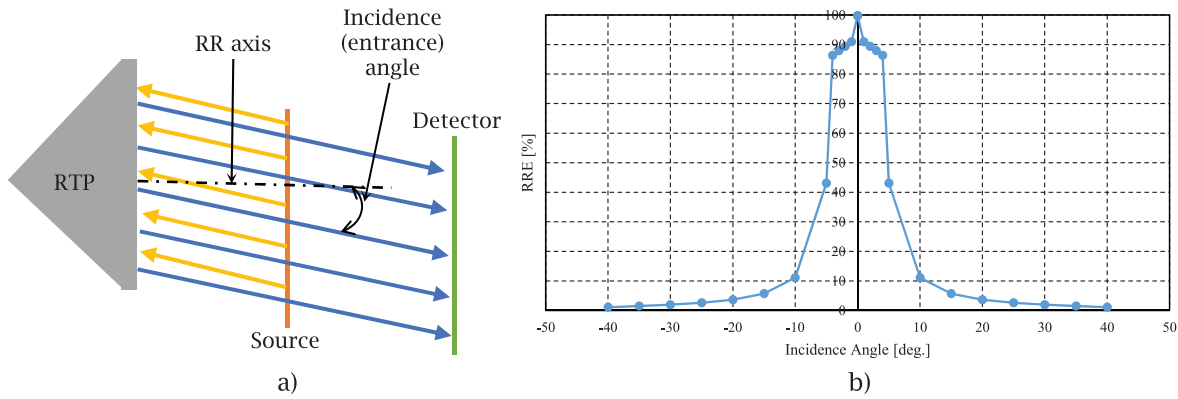


Figure 3. Optical performance of the RTP: a) optical simulation setup, and b) optical simulation results.

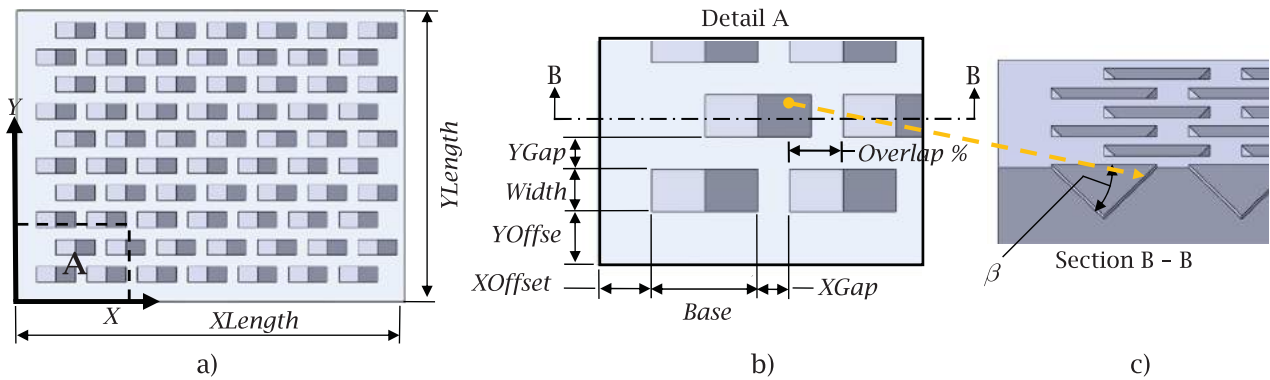


Figure 4. Geometrical parameters of the RTP array: a) top view of an RTP array, b) bottom left corner of the array (detail A in subfigure a), and c) cross section through RTPs (B-B plane in subfigure b).

To rapidly generate arrays belonging to the same family, a Visual Basic script/macro was created under the SolidWorks environment (Fig. 5). The program collects all input parameters outlined in Fig. 4 from a text file and

then generates the geometry of the RTP array according to the preset design constraints and rules.

At first, the program first extrudes the base geometry, an operation that is followed by the calculation of

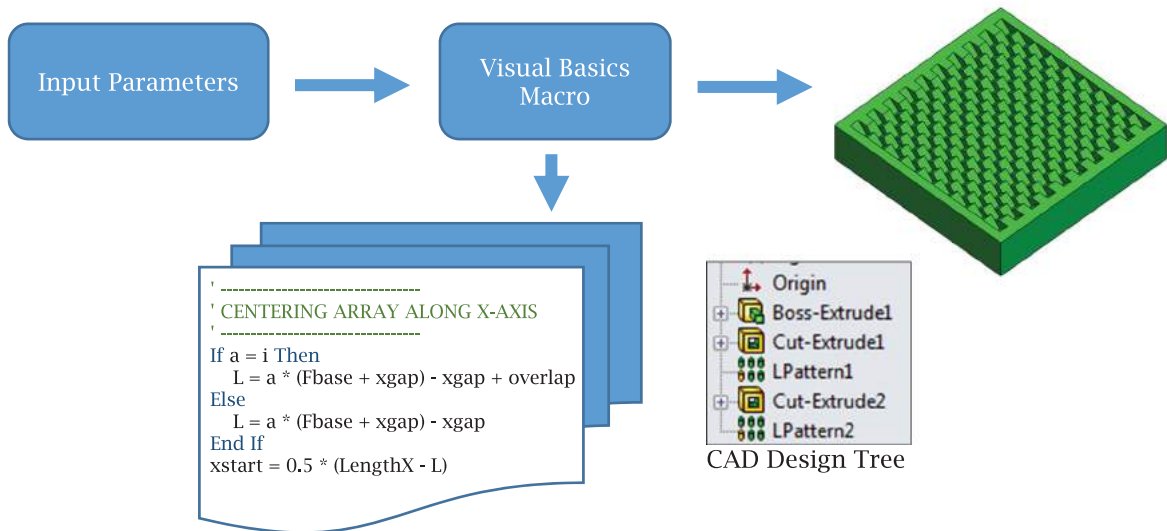


Figure 5. Automatic generation of the RTP array.

the number of structures required to create the array while satisfying the input parameters. After that, the position of the first element is determined in order to ensure that the entire array is centered on the base geometry. Finally, a cut-extrude feature combined with a linear pattern is used to replicate the base RTP element in order to generate the entire array.

2.3. Optical performance of the RTP array

The procedure outlined in the section allows rapid generation of arrays with different geometric characteristics. As such, a family of RTP array geometries were investigated in an attempt to determine the correlation between their geometrical parameters and their optical performance. The two main parameters that were varied for this study were the width and the base of individual RTP elements, while all other parameters were set at constant values as follows: $XOffset = 0$ mm, $YOffset = 0$ mm, $XGap = 0$ mm, $YGap = 0$ mm, $Overlap\% = 50\%$, $XLength = 10$ mm, $YLength = 10$ mm, and $b = 45^\circ$. Numerical simulation was performed on the arrays and their RRE was measured. For all optical simulations, the light was directed towards the RTP at a 0° incidence angle and all setups were absolutely identical. It can be noticed that although the RTPs covered a base flat area of identical dimensions ($10\text{ mm} \times 10\text{ mm}$), the detector measured different RREs for different RTP sizes. This variation can be regarded as a consequence of the changes in the effective RR area defined as the total area of the reflective facets that participate in the retroreflection. The results presented in Fig. 6 clearly indicate that with the exception of the single (e.g. non-arrayed) RTP feature covering the entire base flat surface, an inverse proportionality relationship exists between the total effective RR area and the size/number of arrayed RTP elements.

To further reiterate this dependence between array design and its associated optical performance, the numerical values of few significant optical/geometrical parameters were summarized in Tab. 1.

To further explain this behavior, Fig. 7 depicts two representative cases of RTP array design along with the distribution of the reflected light as recorded by the detector. As it can be noticed, while absolutely no loss of light exists in case of the single RTP (Fig. 7b), certain “dead spots” (e.g. non-retroreflective facets/RTPs) will exist in case of arrayed RTPs (Fig. 7d), particularly for the elements located on the boundary of the base surface. As the summated area of the “dead spots” decreases with the size of the elementary RTP, it becomes clear that this will translate into corresponding retroreflectivity increases. Given that the $Overlap\%$ parameter (Fig. 4) was assumed at 50%, it is inevitable that some of the RTP facets will fall outside of the base $10\text{ mm} \times 10\text{ mm}$ area.

Based on the considerations above, it becomes apparent that while the absolute best scenario from an optical perspective would be a singular RTP instance, this would be in fact unfeasible for manufacturing/applicability reasons. Because of this, a more practical suggestion would be to decrease the size of the RTP as much as possible, one inherent limitation being the width of the cutting tool to be used for RTP array fabrication.

Table 1. Summary of geometrical and optical characteristics of the RTP array.

Base [mm]	Width [mm]	Total Reflective Facets Area [mm ²]	Total Effective RR Area [mm ²]	RRE [%]
10	10	1	141.42	99.99
5	5	3	141.42	76.88
2	2	22	141.42	88.90
1	1	95	141.42	95.37
0.5	0.5	390	141.42	97.68

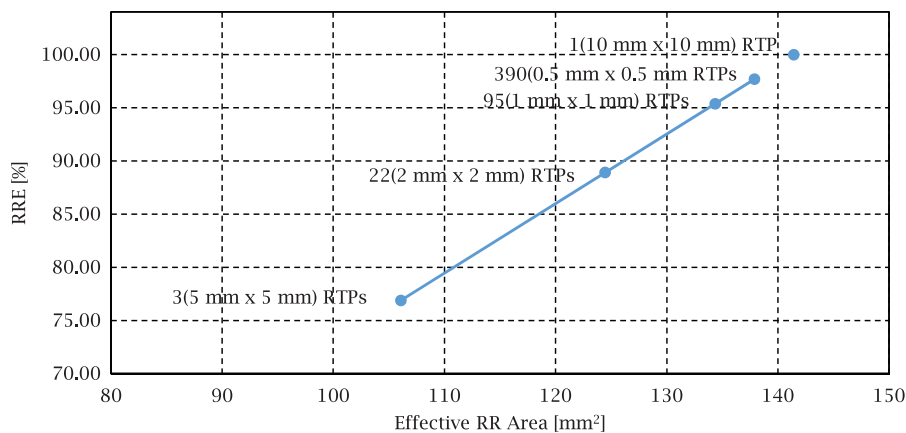


Figure 6. Correlation between the optical performance and the number of arrayed RTP elements.

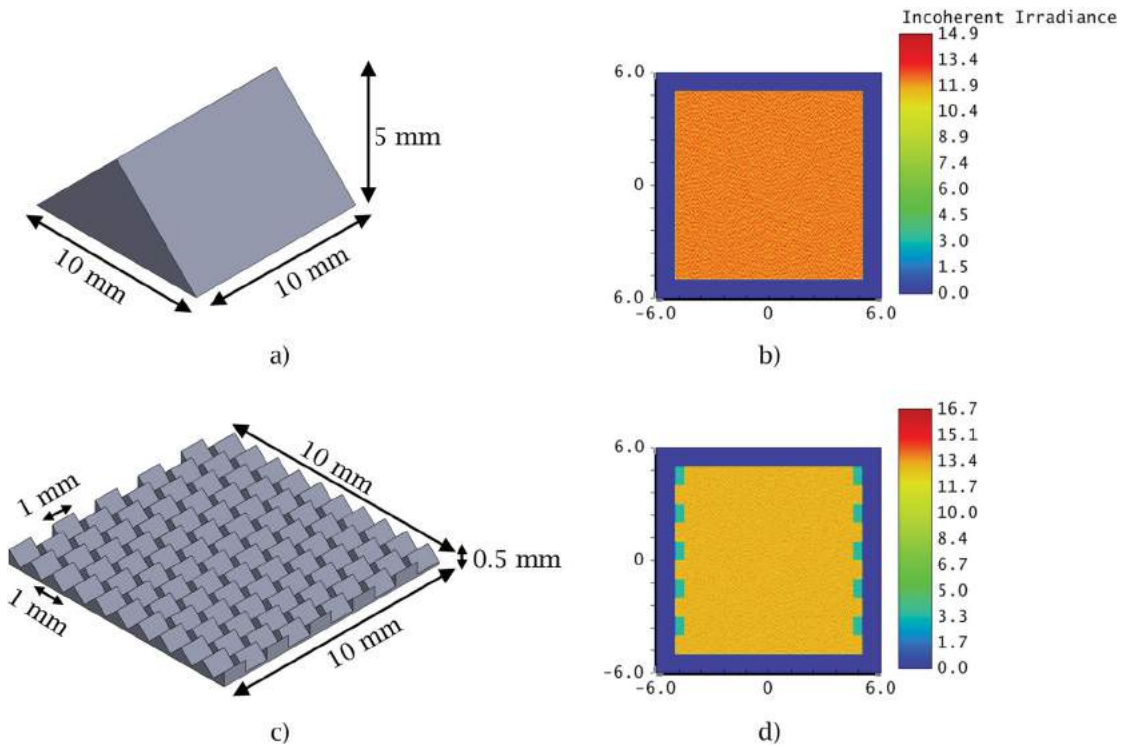


Figure 7. Optical performance of the arrayed RTPs: a) single RTP design, b) retroreflected light distribution for the analyzed single RTP, c) design of an RTP array, and d) retroreflected light distribution for the analyzed RTPs array.

3. Fabrication of the RTP array through $3\frac{1}{2}$ -axis machining

3.1. Diamond cutting tool

To fabricate the intended RTP array, a custom tool was developed and manufactured for use in USPIC operations. The cutter consists of a steel shank and a diamond tip and shares many design characteristics with cutting tools used in parting or turning operations, the primary difference being that clearance and rake faces were positioned in a rather reversed manner (Fig. 8). The use of a diamond tip – that is specific to ultraprecise machining operations – is meant to ensure an optical quality on the retroreflective facets of the RTP [10]. If the surface finish is below the optical quality, the reflective facets will tend to scatter light and this will decrease the reflective efficiency of the

elementary RTP and implicitly that of the array. In this context, it is perhaps worth to mention that while in the traditional pin-bundling-based technique the surface finish is primarily determined by the lapping operation applied on the forming end of the hexagonal pin, the quality of RTP facets is mainly dependent on the overall tool-workpiece interaction/dynamics during USPIC.

In this regard, since USPIC mechanics is somewhat similar to that of turning, the design of the USPIC tool has to adhere to comparable guidelines. As shown in Fig. 9, three angles are critical for the entire cutting geometry: relief/clearance, wedge, and rake.

The relief angle is formed between the post-machined surface of the workpiece and the clearance face of the tool. Its presence is meant to reduce/eliminate the risk of post-machining surface damage [14]. Typical relief

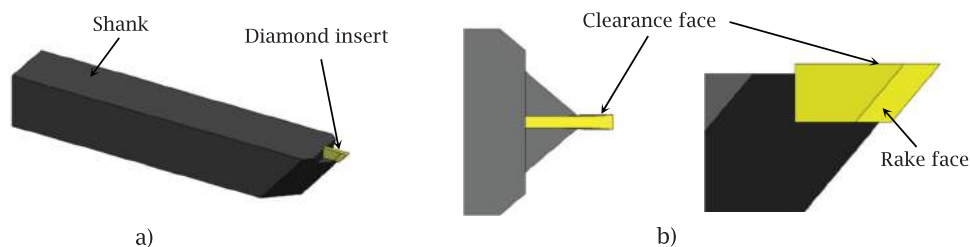


Figure 8. Design of the diamond cutting tool: a) overview of the cutting tool, and b) constructive detail of the tool tip.

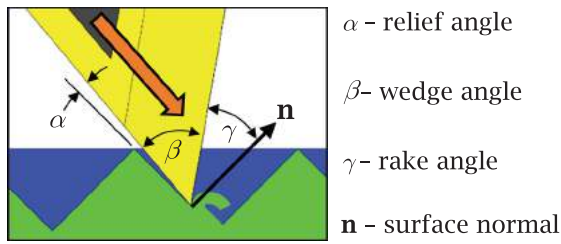


Figure 9. Cutting geometry and tool angles.

angles range from 5° to 15° depending on cutting conditions, tool material, and workpiece material.

On the other hand, the rake angle is measured between a normal to the post-machined surface that passed through the tool tip and the rake face of the tool. According to conventional machining theory, the rake angle determines how the chip develops during the cutting process in a sense that a positive angle (Fig. 9) is associated with decreased cutting forces leading to an improved tool life [9,14]. Since rake angle values are largely determined by the material being cut, values between 0° and 30° are typically recommended [3,9]. Finally, the wedge angle is determined as the 90° complement of rake and relief angles ($\alpha + \beta + \gamma = 90^\circ$). As such, a large wedge angle (i.e. close to 90°) is associated with a stiff tool, while a smaller wedge angle makes the cutter more susceptible to failure.

Similar to turning, the radius of the cutting edge (r_β) has strong effect on the surface finish as well as the durability of the tool [10]. The tool used in RTP cutting operations is characterized by a 50° degree wedge angle which in turn enables a wide range of rake and clearance angles. Based on the considerations presented in Section 2.2, the tool was fabricated with a width of 1 mm in an attempt to maintain the RTP structures dimensionally comparable to their ICC equivalents that are commonly used in automotive lighting applications. To minimize the presence of “dead” (e.g. unreflective) zones of the RTP facets around the apex, the radius of the cutting edge was reduced to the minimum attainable value ($r_\beta \approx 0$).

3.2. Cutting motions and strategies

When it comes to the fabrication of an RTP array, different cutting strategies can be imagined. The “unidirectional” strategy that was previously [6] introduced for individual RTPs consists of a combination of plunging and ploughing motions. The primary difference between the two main types of motions consists in the relative position between the tool and the workpiece (Fig. 10). Evidently, while the large positive rake angle associated with the plunging motion facilitates chips evacuation, its negative value –characteristic to a

ploughing cut – will translate into a decreased quality on the corresponding RTP facet. Furthermore, the increased cutting forces make the cutter more susceptible to failure during ploughing.

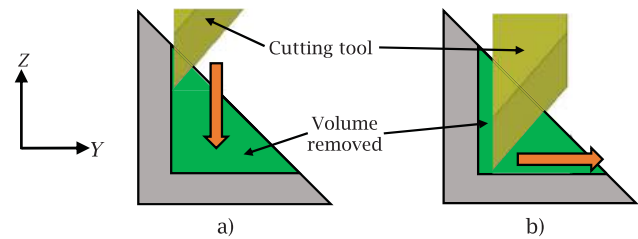


Figure 10. Principal motions in unidirectional RTP cutting: a) plunging, and b) ploughing.

Figure 10b suggests that in order to achieve ideal cutting conditions on the second RTP facet, the tool should be in fact rotated in a counterclockwise direction by 90° . However, this position is geometrically unfeasible, such that other cutting strategies have to be used in order to overcome the aforementioned drawbacks of the ploughing motion, possibly by involving plunging motions only. On the other hand, the main advantage of this unidirectional approach resides in the fact that repositioning (through rotation) of the workpiece is not necessary, such that three-axis kinematics was sufficient to generate the intended RTP array geometry.

To further improve the roughness of both facets of the RTP, a novel cutting strategy was developed in the context of the current study. According to this new technique, the cutting starts by roughing out the cavity of the RTP element in a unidirectional manner similar to the one depicted in Fig. 11. It is important to note that – if the RTPs are to cut on a base flat surface, the workpiece should be held in a rotated ($A = 45^\circ$). With the exception of a small portion at the beginning of the cut, roughing consists of a four-step sequence comprised of two cutting and two ancillary motions required to position the tool for the next cutting cycle. During roughing, the horizontal cutting motion has to exceed the thickness of the layer being cut (l) in order to ensure a successful chip separation. Evidently, the length of the cutting increases as the roughing progresses.

Once the near-net shape of the RTP is achieved, a cut performed solely by means of plunging was used to finish the facet that has been previously subjected to ploughing only. In order to implement the finish strategy, an appropriate machine tool setup and/or calibration was critical in obtaining the intended optical surface quality [3]. For this purpose, the tool was installed by ensuring the parallelism between the clearance face and the XZ plane of the multi-axis machine tool. Since

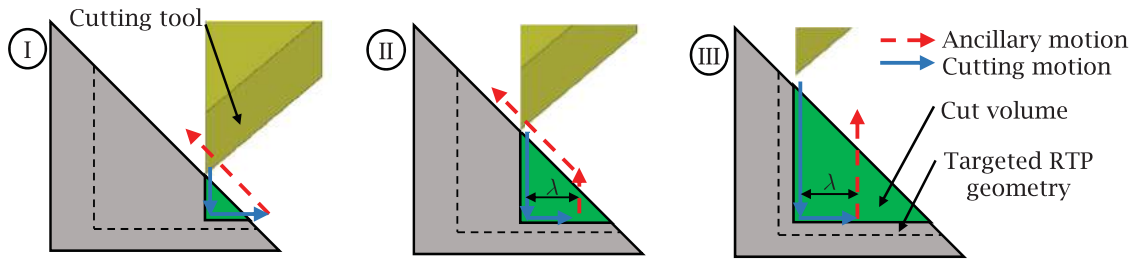


Figure 11. Roughing sequence.

similar strict parallelism conditions were also enforced between the cutting edge and the X-axis of the machine, an adjustable cutting tool fixture was designed and used for this purpose. In order to orient the horizontal facet – that was roughed out through ploughing – in a vertical position, workpiece rotation is mandatory, such that a five-axis machine tool with rotary table configuration was employed for this purpose (Fig. 12). However, since the rotational axes have merely a positioning/indexing role, the proposed strategy resembles a traditional $3\frac{1}{2}$ -axis machining operation that is also sometimes termed as $3 + 2$, inclined, fixed, or tilted machining [1,4,13]. The addition of the rotary axes necessitates the development of a complete kinematic model of the five-axis machine tool. Its development constitutes a routine analysis in the broader context of five-axis machining postprocessors, especially since generalized kinematic models have also been proposed [12,15].

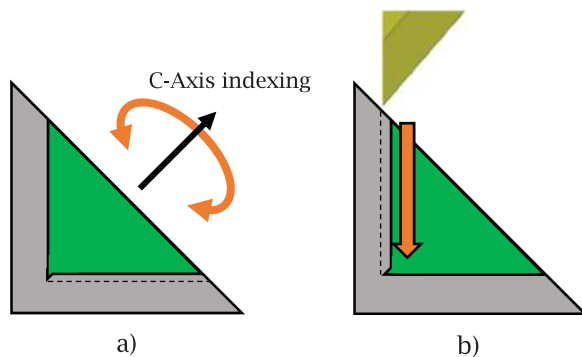


Figure 12. Finishing sequence performed on a roughed-out RTP: a) indexing motion, and b) finishing cut.

3.3. Machine tool kinematics

In general terms, a five-axis machine tool provides additional manufacturing flexibility through the addition of two rotational degrees of freedom that supplement the three translational degrees that are offered by a classical three-axis machine. According to the terminology introduced in [15], an AC rotary table five-axis micro-machine was used to demonstrate the newly-developed $3\frac{1}{2}$ -axis cutting strategy. Similar to prior naming

conventions, A represents the primary, while C is the secondary rotary axis.

According to the robotics theory, an inverse kinematics transformation is required in order to convert the position \mathbf{P}^W of the cutting point from the workpiece coordinate system (WCS) into a point \mathbf{P}^M located in the machine coordinate system (MCS):

$$\mathbf{P}^M = {}^M_W \mathbf{T} \cdot \mathbf{P}^W \quad (1)$$

where ${}^M_W [\mathbf{T}]$ represents the generalized coordinate transformation matrix from WCS to MCS [15].

As illustrated in Fig. 13, each joint connects different links of the kinematic chain [2,15], and in turn each of the joints is associated with one of the five degrees of freedom. The relative position between successive joints is determined by the positional matrices \mathbf{b}_i , while the relative orientation between them is quantified by means of the rotational matrices \mathbf{R}_i . As such, the kinematic chain depicted in Fig. 13 can be described by means of four position vectors (e.g. \mathbf{b}_0 , \mathbf{b}_1 , \mathbf{b}_2 , and \mathbf{b}_3), and two rotational matrices (e.g. \mathbf{R}_X and \mathbf{R}_Z). In general terms, \mathbf{b}_i can be described as:

$$\mathbf{b}_i = \begin{bmatrix} 1 & 0 & 0 & x_i \\ 0 & 1 & 0 & y_i \\ 0 & 0 & 1 & z_i \\ 0 & 0 & 0 & 1 \end{bmatrix} \quad (2)$$

while the general rotation matrix \mathbf{R}_i about an arbitrary vector in space $\mathbf{n}^t = [n_x \ n_y \ n_z]$ is [17]:

$$\mathbf{R}_i = \begin{bmatrix} n_{x_i}^2 v\theta + c\theta & n_{x_i} n_{y_i} v\theta - n_{z_i} s\theta & n_{x_i} n_{z_i} v\theta + n_{y_i} s\theta & 0 \\ n_{x_i} n_{y_i} v\theta + n_{z_i} s\theta & n_{y_i}^2 v\theta + c\theta & n_{y_i} n_{z_i} v\theta - n_{x_i} s\theta & 0 \\ n_{x_i} n_{z_i} v\theta - n_{y_i} s\theta & n_{y_i} n_{z_i} v\theta + n_{x_i} s\theta & n_{z_i}^2 v\theta + c\theta & 0 \\ 0 & 0 & 0 & 1 \end{bmatrix} \quad (3)$$

For both Eqs. 2 and 3, i is the index of the joint, q is the rotational angle around the \mathbf{n}_i vector, while the other expressions are simplified trigonometric forms: $c\theta = \cos \theta$, $s\theta = \sin \theta$, $v\theta = 1 - \cos \theta$.

It is important to emphasize here that while rotational matrices can be reduced to much simpler expressions,

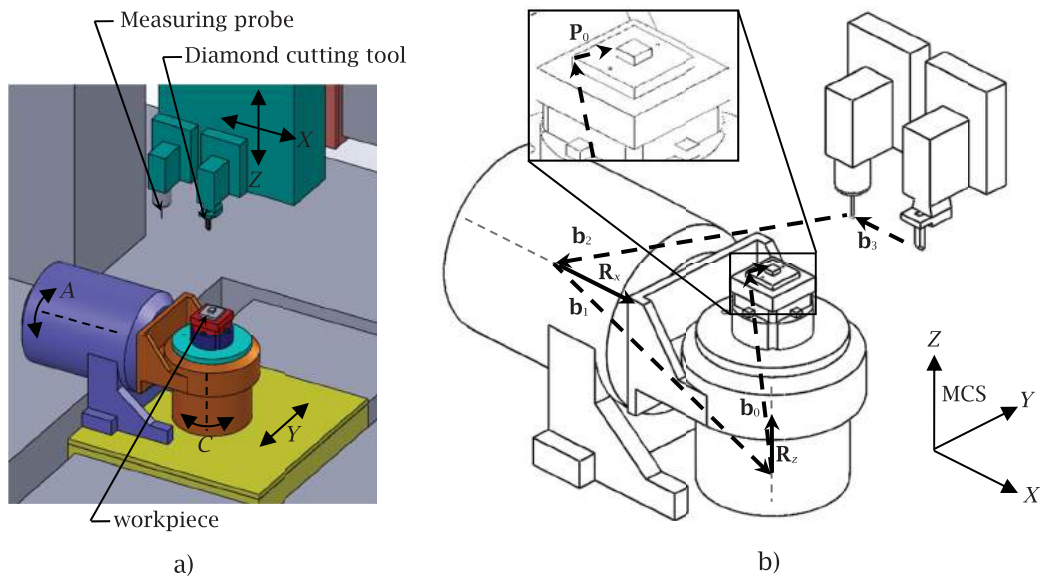


Figure 13. Five-axis micromachine: a) motions, and b) inverse kinematics model.

the inherent precision required for the RTP fabrication operation requires a careful account of the misalignments that are present along the kinematic chain. In line with this thought, after the completion of the calibration routines, it was found that the actual cosine directors of the two rotational axes of the machine were:

$$\delta \mathbf{n}_{R_X}^t = [0.999995 \quad -0.0014502 \quad 0.00268292] \quad (4)$$

and

$$\delta \mathbf{n}_{R_Z}^t = [-0.00015666 \quad 0.00048007 \quad 0.99999987] \quad (5)$$

which are close, but without being coincident with their theoretical values, *i.e.* $[1 \ 0 \ 0]$ and $[0 \ 0 \ 1]$, respectively.

Based on all the above considerations, a more detailed form of the generalized coordinate transformation matrix used in Eqn. (1) can be written as:

$${}^M_W \mathbf{T} = \mathbf{b}_3 \cdot \mathbf{b}_2 \cdot \mathbf{R}_X \cdot \mathbf{b}_1 \cdot \mathbf{R}_Z \cdot \mathbf{b}_0 \quad (6)$$

which constitutes in fact the core of the required inverse kinematics transformation.

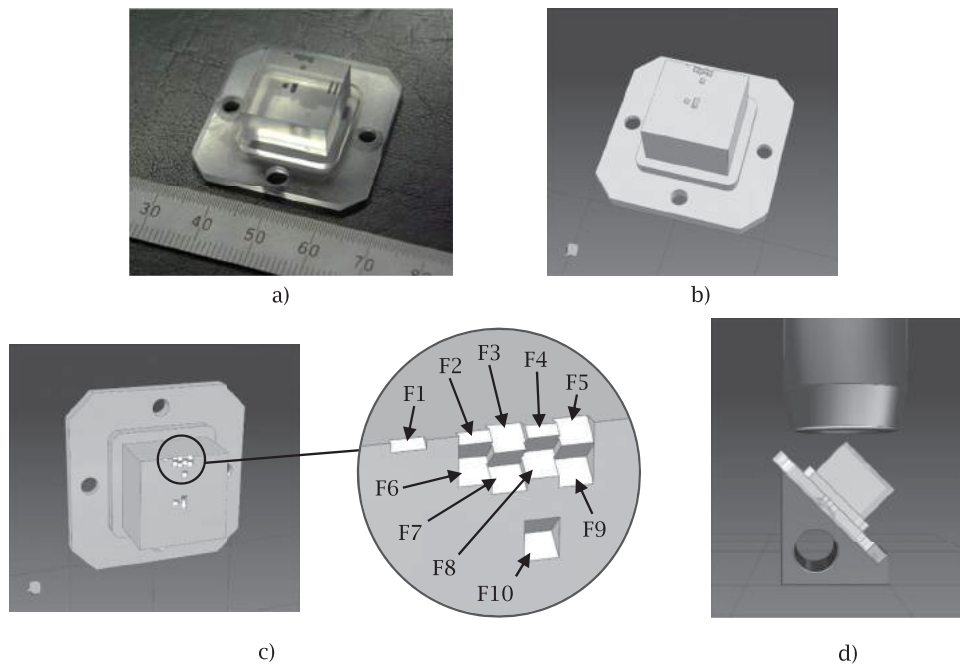


Figure 14. RTP elements generated for validation purposes: a) physical test workpiece, b) CAD-rendered workpiece, c) facet labeling for roughness assessment, and d) relative positioning between the workpiece and microscope objective.

4. Experimental validation

To test the proposed fabrication approach, several RTP features were machined on a top flat face of a PMMA block (Figs. 14a, 14b). The feed rates used for roughing and finishing varied between 100 mm/min and 10 mm/min, while the corresponding layer thicknesses were selected at 10 μ m and 1 μ m, respectively. Since the primary goal of the experimental validation was to assess the quality of the fabricated RTP elements (Figs. 14c, 14d), no enlarged arrays were generated at this time. Instead, the majority of the RTPs were located in positions that can be placed at the appropriate focal distance for the optical profilometer used for surface roughness evaluation (Fig. 14d).

A summary of the surface quality results obtained during trials is presented in Tab. 2. According to these values, $S_a = 147.07 \pm 41.37$ nm for all 10 assessed facets.

Table 2. Quality of the fabricated RTP facets.

Facet	Average Areal Surface Roughness S_a [nm]	Facet	Average Areal Surface Roughness S_a [nm]
F1	191.28	F6	121.63
F2	190.36	F7	90.19
F3	109.21	F8	114.40
F4	179.54	F9	114.46
F5	201.36	F10	158.26

A more in-depth analysis of the surface quality reveals significant differences between the original unidirectional approach (Fig. 15) and the proposed $3\frac{1}{2}$ -axis cutting technique (Fig. 16). As a general comment, the quality of the facets obtained through plunging seems to be more than 4 times better than that obtained through ploughing. Beyond that, even if the cutting process seems to be somewhat difficult to stabilize at this time ($90.19 \text{ nm} \leq S_a \leq 191.28 \text{ nm}$), its quality can be brought close to the optical quality (Fig. 16c).

One of the largest contributors to the significant decreases in surface quality was represented by the occurrence/development of chips on the cutting edge that in turn have translated into veritable scratches/grooves on the surface of the RTP facets (Fig. 17). While the rationale behind their formation remains at this time unclear, it is possible that they have appeared due to a combination of incorrectly sharpened tool edge and/or workpiece material build-up. The size of the chips/scratches varies, but most of them remain below 5 μ m wide while their length stretches over the entire RTP facet.

As a final verification of their optical functionality, the fabricated RTP elements were subjected to an incident light that was projected from the back of the workpiece (Fig. 18). This setup mimics the real working scenario in which the RTPs will be used, as the

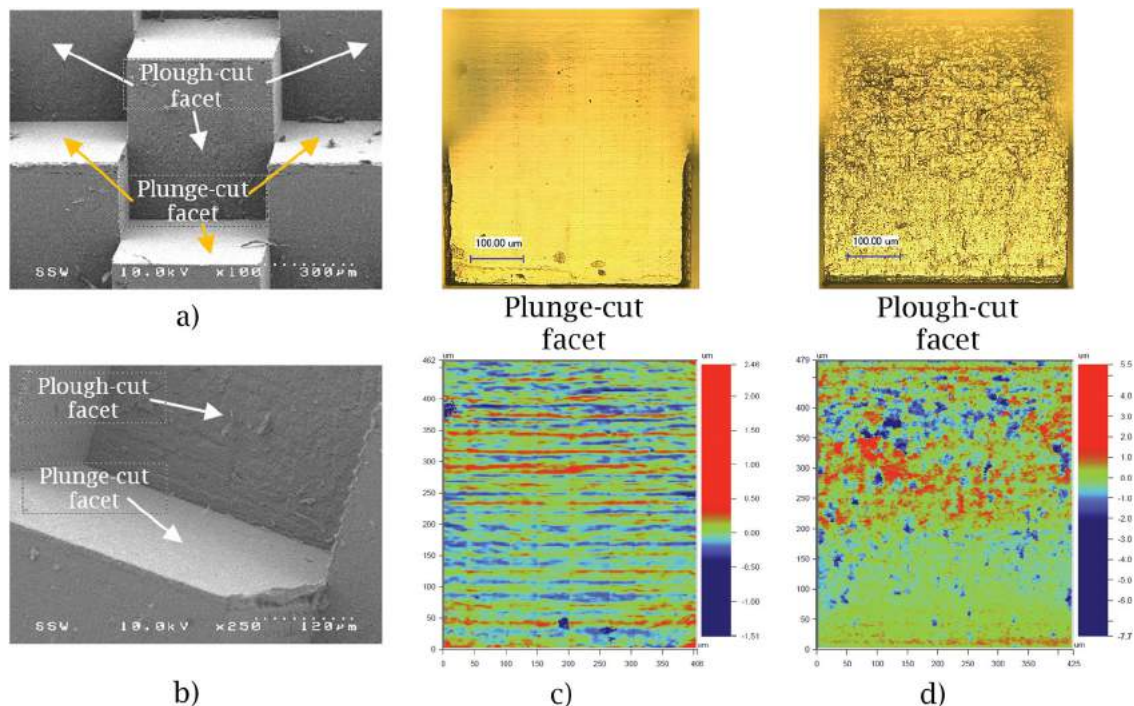


Figure 15. Quality of the unidirectional cutting: a) broad-field SEM micrograph, b) close-up SEM micrograph, c) optical (top) and topographic (bottom) images of the plunge-cut facet ($S_a = 114.55$ nm), and d) optical (top) and topographic (bottom) images of the plough-cut facet ($S_a = 468.19$ nm).

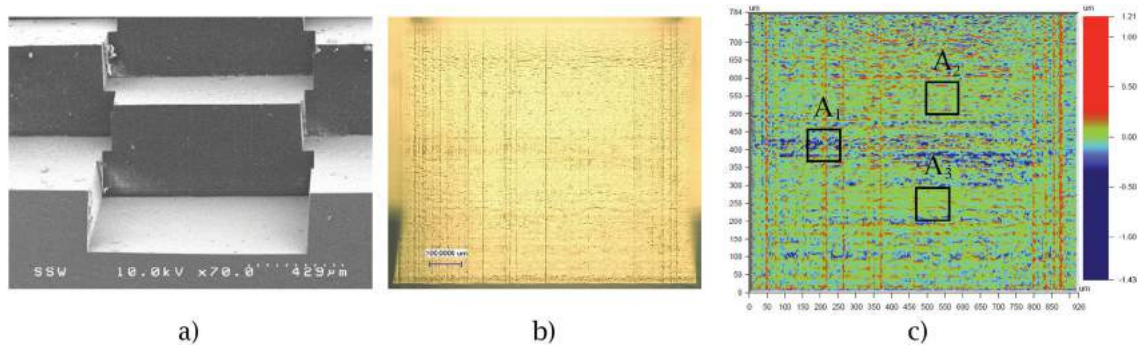


Figure 16. Quality of the $3\frac{1}{2}$ -axis cutting: a) broad-field SEM micrograph, b) optical image of facet F7 ($S_d = 90.19$ nm), and c) topographic image of facet F7 ($S_{dA_1} = 120.23$ nm, $S_{dA_2} = 70.56$ nm, $S_{dA_3} = 50.63$ nm).

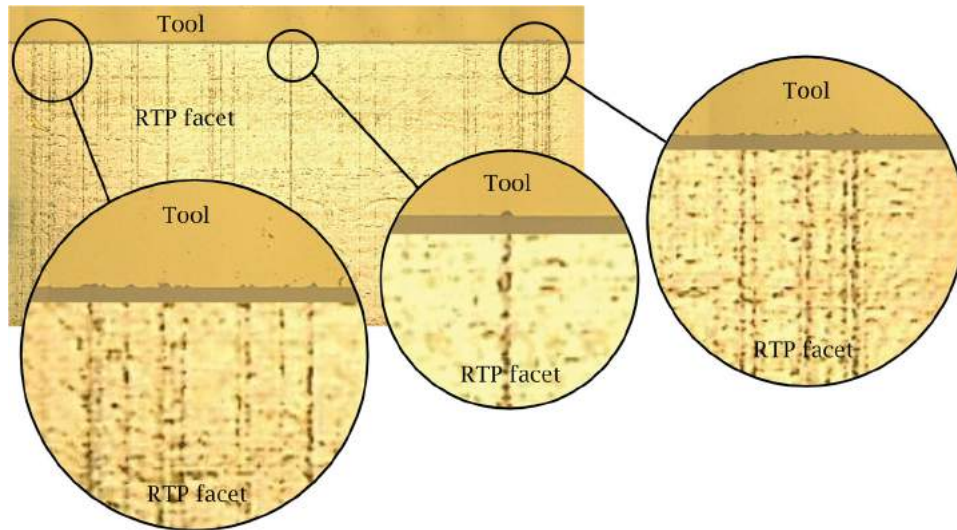


Figure 17. RTP facet scratches caused by chipping of the diamond tool cutting edge.

machined facets constitute in fact the “negative” (e.g. mold insert) of the final optical element. While it is true that this rather simplistic experiment can only provide a certain level of qualitative evaluation of the RTPs – at this time – it was considered that this is sufficient to demonstrate that the proposed technique can generate functional optical elements that are visible under

a wide incidence angle – a desirable trait in safety applications.

5. Conclusions

The primary objective of this study was to further enhance the unidirectional cutting technique that was

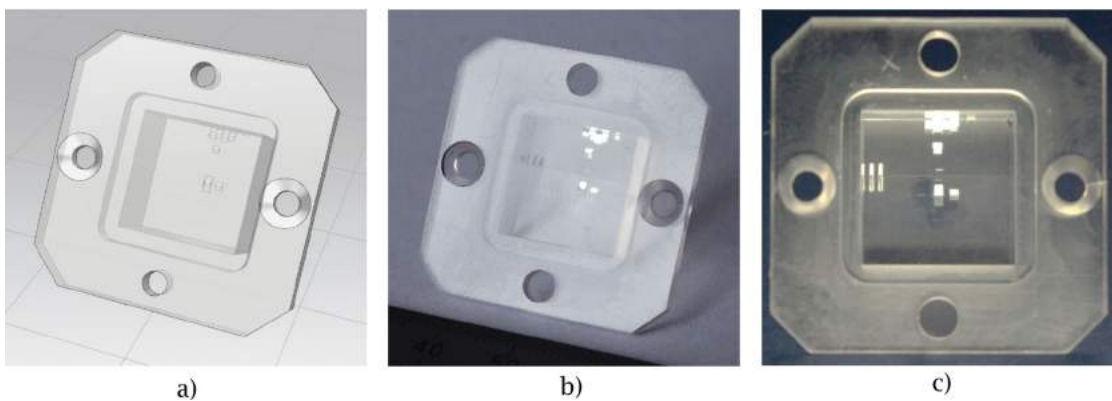


Figure 18. Optical functionality of the fabricated RTP: a) CAD-rendered image of the workpiece, b) lateral illumination, and c) normal-to-aperture illumination.

previously proposed for fabrication of the RTPs. Since the only way to further improve the quality of the RTP facets is by producing them exclusively by means of plunge-cutting, a new 3½-axis USPIC technique was developed for this purpose.

However, prior to being considered for fabrication, an automatic CAD-based procedure was devised to quickly generate parametrized RTP arrays that were then subjected to optical simulations in order to determine an optically-performant size for them. Following this, an inverse kinematics model of the five-axis machine used during cutting experiments was developed and its numerical parameters were adjusted according to the data collected through calibration experiments. The experiments performed revealed that the proposed 3½-axis cutting technique can generate RTP facets with average areal roughness around 150 nm that in some cases can be as low as 50 nm. The RTP elements that were produced by means of the new approach proved to be optically functional.

In summary, the proposed 3½-axis USPIC technique has proved to be a viable fabrication option for the RTP elements. Future work will attempt to improve further the quality of the retroreflective facets, as well as to improve the productivity of the overall manufacturing process.

Acknowledgements

This study is the result of collaboration between the Western University in London, Ontario and National Research Council of Canada in London, Ontario. Partial financial support was also provided by the Natural Sciences and Engineering Research Council (NSERC) of Canada and AUTO21 Network of Centers of Excellence. The authors would also like to acknowledge CMC Microsystems for the provision of the optical simulation software that has been used in this study.

ORCID

Benjamin Hamilton  <http://orcid.org/0000-0003-0970-2458>
 Sama Hussein  <http://orcid.org/0000-0002-6024-3237>
 Nicolas Milliken  <http://orcid.org/0000-0003-1463-0452>
 O. Remus Tutunea-Fatan  <http://orcid.org/0000-0002-1016-5103>
 Evgueni V. Bordatchev  <http://orcid.org/0000-0003-2347-6338>

References

- [1] Albert, M.: An Overview of 3+2 Machining, *Modern Machine Shop*, 79, 2006, 94–97. <http://www.mmsonline.com/articles/an-overview-of-3-2-machining>
- [2] Boz, Y.; Lazoglu, I.: A Postprocessor for Table-Tilting Type Five-Axis machine Tool Based on Generalized Kinematics with Variable Feedrate Implementation, *Advanced Manufacturing Technology*, 66, 2013, 1285–1293. <http://dx.doi.org/10.1007/s00170-012-4406-7>
- [3] Brinksmeier, E.; Gläbe, R.; Schönemann, L.: Diamond Micro Chiseling of Large-Scale Retroreflective Arrays, *Precision Engineering*, 36, 2012, 650–657. <http://dx.doi.org/10.1016/j.precisioneng.2012.06.001>
- [4] Chen, Z.C.; Dong, Z.; Vickers, G.W.: Automated Surface Subdivision And Tool Path Generation For 3½-Axis CNC Machining Of Sculptured Parts, *Computers in Industry*, 50, 2003, 319–331. [http://dx.doi.org/10.1016/S0166-3615\(03\)00019-8](http://dx.doi.org/10.1016/S0166-3615(03)00019-8)
- [5] Evonik Industries: Machining Plexiglas: Guidelines for Workshop Practice, 2009. https://www.plexiglas-shop.com/pdfs/en/311-1%20Machining%20PLEXIGLAS%C2%AE_en.pdf
- [6] Hamilton, B.; Hussein, S.; Tutunea-Fatan, O.R.; Bordatchev, E.V.: Fabrication of Right Triangular Prism Retroreflectors through Ultraprecise Single Point Inverted Cutting, *Proceedings of the ASME 2016 11th International Manufacturing Science and Engineering Conference (MSEC 2016)*, Jun. 2016, Blacksburg, USA, Vol. 2, paper MSEC2016-8715, pp. V002T04A046, 11 pages. <http://dx.doi.org/10.1115/MSEC2016-8857>
- [7] Hussein, S.; Hamilton, B.; Tutunea-Fatan, O.R.; Bordatchev, E.V.: Novel Retroreflective Micro-Optical Structure for Automotive Lighting Applications, *SAE International Journal of Passenger Cars – Mechanical Systems*, 9, 2016, 10 pp. <http://dx.doi.org/10.4271/2016-01-1407>
- [8] Nilsen, R. B.; Lu, X. J.: Retroreflection Technology, *SPIE*, 5616, 2004, 47–60. <http://dx.doi.org/10.1117/12.577624>
- [9] Oberg, E.; Jones, F.; Horton, H., Ryffel, H.: *Machinery's Handbook 28th Edition*, 2008, Industrial Press, New York, 733–738.
- [10] Schönemann, L.; Brinksmeier, E.; Flucke, C.; Gläbe, R.: Tool-Development for Diamond Micro Chiseling, *Proceedings of the Euspen International conference – Delft*, 2010.
- [11] Seward, G.: Measurement and Characterization of Angular Reflectance for Cube-Corners and Microspheres, *Optical Engineering*, 38, 1999, 164–169. <http://dx.doi.org/10.1117/1.602077>
- [12] She, C.; Chang, C.: Design of a generic five-axis postprocessor based on generalized kinematics model of machine tool, *International Journal of Machine Tools & Manufacture*, 47, 2007, 537–545. <http://dx.doi.org/10.1016/j.ijmactools.2006.06.002>
- [13] Suh, S.H.; Lee, J.J.: Five-axis part machining with three-axis CNC machine and indexing table, *ASME Journal of Manufacturing Science and Engineering*, 120, 1998, 120–128. <http://dx.doi.org/doi:10.1115/1.2830087>
- [14] Stephenson, D.; Agapiou, J.: *Metal Cutting Theory and Practice Second Edition*, Taylor and Francis, Boca Raton, 2006, 512–514, Ch. 9.
- [15] Tutunea-Fatan, O.R.; Feng, H.S.: Configuration Analysis of Five-Axis Machine Tools Using a Generic Kinematic Model, *Machine Tools & Manufacture*, 44, 2004, 1235–1243. <http://dx.doi.org/10.1016/j.ijmactools.2004.03.009>
- [16] Van Arnem, D. 1978, Method for Forming Retroreflective Sheeting, U.S. Patent 4243618. <https://www.google.com.ar/patents/US4243618>
- [17] Zeid, I.: *Mastering CAD/CAM*, McGraw-Hill, New York, 2005.